Demonstration and structural basis of a therapeutic DNA aptamer for SARS-CoV-2 spike protein detection

Yujun Liu[a,b †], Kaidong Wang[c,d,f†], Weiguang Wang[a,b], Saarang Kashyap[a,b], Jonathan Jih[a,b,e], Anthony Imani[a,b], Tzung Hsiai[c,d,f], Z. Hong Zhou[a,b,e*]

[a]California NanoSystems Institute, University of California at Los Angeles, Los Angeles, 90095, California, USA

[b]Department of Microbiology, Immunology and Molecular Genetics, University of California at Los Angeles, Los Angeles, 90095, California, USA

[c]Division of Cardiology, Department of Medicine, David Geffen School of Medicine, University of California Los Angeles, Los Angeles, California 90095, USA

[d]Department of Medicine, Greater Los Angeles VA Healthcare System, Los Angeles, California 90073, USA

[e]Molecular Biology Institute, University of California, Los Angeles (UCLA); Los Angeles, CA 90095, USA.

[f]Department of Bioengineering, Henry Samueli School of Engineering and Applied Science, University of California Los Angeles, Los Angeles, California 90095, USA

*Corresponding authors:

　　　　Email: Hong.Zhou@ucla.edu (Z.H.Z.)

[†]YL and KW contributed equally as first authors

KEYWORDS: Aptamer, cryo-EM, SARS-CoV-2, receptor binding domain, detection**,** specificity

Abstract

At the onset of the COVID-19 pandemic, the absence of a rapid and highly specific diagnostic method for the SARS-CoV-2 virus led to significant delays in detection, adversely affecting clinical outcomes. This shortfall highlights the urgent need for adaptable, scalable, and reusable diagnostic technologies to improve future pandemic responses. To address this challenge, we developed a renewable electrochemical impedance biosensor device employing a synthetic nucleotide-based therapeutic aptamer (termed 'aptasensor') targeting the SARS-CoV-2 spike (S) protein receptor-binding domain (RBD). We demonstrate that our aptasensor can detect the Omicron BA.2 S protein within one hour and possesses concentration-dependent sensitivity at biologically relevant levels. Notably, the aptasensor is reusable after regeneration by a simple pH 2 buffer treatment. Aptamer binding to the S protein was confirmed by immunogold labeling and visualization by negative-stain electron microscopy. We used cryogenic electron microscopy (cryo-EM) to resolve high-resolution maps of the S protein in both the open and closed conformations and characterized aptamer binding to the up RBD in the open conformation. Taken together, these results establish the versatility and scalability of aptamer-based biosensors, presenting them as a potential transformative diagnostic platform for emerging pathogens. This combination of rapid detection, specificity, and renewable capabilities in a single diagnostic solution marks a significant advance in pandemic preparedness.

1. Introduction

The SARS-CoV-2 virus, a single-stranded positive-sense RNA virus of the *Coronaviridae* family, encodes four structural proteins in its genome: spike (S), envelope (E), membrane (M), and nucleocapsid (N) (Hoffmann et al. 2020; Walls et al. 2020). Among these, the S protein plays a central role in viral entry into host cells. It assembles as a homotrimer, with each monomer consisting of two functional subunits: S1, which binds to receptors, and S2, which mediates membrane fusion (Cai et al. 2020; Wrapp et al. 2020). The receptor-binding domain (RBD) within the S1 subunit specifically binds to the human angiotensin-converting enzyme 2 (hACE2) receptor and alternates between "open" and "closed" conformations (Shang et al. 2020), balancing receptor engagement with immune evasion. Following RBD binding to hACE2, the S2 subunit undergoes proteolytic activation by host proteases, exposing the fusion peptide required for facilitating membrane fusion between virus and host cell (Benton et al. 2020; Xia et al. 2020; Yan et al. 2020). These processes underscore the importance of the S protein in viral pathogenesis and its role as a key target for neutralizing antibodies and vaccine development.

The COVID-19 pandemic has emphasized the need for scalable and accurate detection methods to manage viral outbreaks. Current diagnostic approaches include molecular biological detection (e.g., reverse-transcriptase polymerase chain reaction, RT-PCR), immunological assays (e.g., enzyme-linked immunosorbent assays, ELISA), and pulmonary imaging techniques. RT-PCR, the gold standard for molecular detection, provides high sensitivity and specificity in identifying viral RNA but is limited by its dependence on sophisticated infrastructure and susceptibility to mutations in viral target sequences (Artika et al. 2022; Samson et al. 2020). Immunological assays detect viral proteins more rapidly but require specialized equipment and expertise (Khan et al. 2022), while pulmonary imaging methods, such as chest X-rays or computed tomography, are labor-intensive and cost-prohibitive at scale (Shi et al. 2020). These

43 limitations highlight the urgent need for diagnostic technologies that are rapid, accessible, and
44 adaptable to evolving viral threats.

45 Biosensors represent a promising alternative to traditional diagnostic methods. Such
46 sensors convert biological signals into measurable electrical outputs through optical,
47 electrochemical, piezoelectric, or thermal modalities (Justino et al. 2016; Perumal and Hashim
48 2014). These devices offer advantages such as high sensitivity, rapid detection, and potential
49 scalability for point-of-care applications (Pohanka 2018). Their widespread adoption, however, is
50 hindered by challenges such as short operational lifespan, limited reusability, and dependence on
51 multiple devices for signal detection and processing (Patel et al. 2023). Overcoming these
52 obstacles is crucial to unlocking the full potential of biosensors for infectious disease diagnostics.

53 Aptamers have emerged as a transformative solution for biosensor development. These
54 single-stranded nucleic acids, selected through systematic evolution of ligands by exponential
55 enrichment (SELEX), exhibit high-affinity and high-specificity binding to target molecules
56 comparable to antibodies (Sefah et al. 2010). They offer distinct advantages, however, including
57 lower production costs, enhanced chemical stability, and ease of modification (Kumar
58 Kulabhusan et al. 2020). Recent breakthroughs in machine learning have further refined the
59 design and synthesis of aptamers, enabling rapid adaptation to mutations in viral targets (Bashir
60 et al. 2021; Chen et al. 2021). These advancements position aptamers as versatile and scalable
61 solutions for next-generation biosensors, addressing key limitations of traditional diagnostic
62 methods while providing the adaptability needed to counter emergent threats effectively.

63 Among emergent threats, SARS-CoV-2 stands out as a highly mutagenic pathogen that
64 necessitates rapid and precise diagnostic solutions. In this study, we developed a renewable
65 aptamer-based electrochemical impedance biosensor device, termed an aptasensor, to detect the
66 SARS-CoV-2 S protein. Our aptasensor, composed of a thiol-functionalized anti-SARS-CoV-2 S
67 protein aptamer immobilized on gold nanoparticle-modified carbon nanotube electrodes,
68 achieved rapid and dose-dependent detection of the Omicron BA.2 S protein within a short
69 timeframe. To further characterize native aptamer binding, we used cryo-EM to confirm its
70 selective interaction with the open conformation of the S protein and observed no binding in the
71 closed state. Importantly, the aptasensor retained its functionality after simple pH-based
72 regeneration, underscoring its reusability. This innovative design highlights the potential of the
73 aptasensor as a scalable, reusable, and adaptable diagnostic platform for SARS-CoV-2 and other
74 emergent viral threats.

2. Materials and methods

2.1 Reagents

77 Gold (III) chloride hydrate (~52% Au basis), potassium chloride hydrate, sulfuric acid (95.0-
78 98.0%), potassium hexacyanoferrate (II) trihydrate (≥98.5%), potassium ferricyanide (III) (99%),
79 HEPES solution, Tween 20, glycine (≥98.5%), ethanol (≥99.5%), sodium chloride (≥99.0%),
80 phosphate buffer solution (PBS, 1.0 M, pH 7.4), and bovine serum albumin (BSA) were obtained
81 from Sigma-Aldrich. All reagents were chosen for their high purity to ensure consistency and
82 reproducibility in sensor fabrication. Multi-walled carbon nanotubes (XFM01, 5-15 nm in
83 diameter, 10-30 μm in length) were sourced from XFNANO Technology Co. Ltd. The anti-
84 SARS-CoV-2 S protein aptamer CoV2-6C3 (5'- CGC AGC ACC CAA GAA CAA GGA CTG

85   CTT AGG ATT GCG ATA GGT TCG G - 3') (Sun et al. 2021) was synthesized and purified by
86   Integrated DNA Technologies (IDT). Recombinant SARS-CoV-2 S protein (lyophilized and
87   liquid forms) was purchased from ACROBiosystems (SPN-C5227, Newark, DE, USA).
88   Ultrapure water (18.2 MΩ cm) was prepared using a Millipore purification system.

2.2 Electrochemical impedance tests

90   Electrochemical measurements were conducted using a Gamry Interface 1010E workstation
91   (Gamry Instruments, Inc., USA). Electrochemical impedance spectroscopy (EIS) was performed
92   over a frequency range from 100 kHz to 0.1 Hz to capture relevant charge transfer dynamics,
93   using an electrolyte solution containing 0.1 M KCl, and 5 mM $[Fe (CN)_6]^{3-/4-}$. This composition
94   was selected to facilitate electron transfer between the electrode and the analyte. The Randles
95   model was used to fit the EIS data, with charge transfer resistance (R_{ct}) values extracted to
96   evaluate aptamer binding events and sensor performance (Vivier and Orazem 2022).

2.3 Preparation of a label-free electrochemical impedance aptasensor

98   *Carbon Nanotube Dispersion and Electrode Preparation*   A 2 mg/mL suspension of multi-
99   walled carbon nanotubes (CNTs) in a 50:50 (v/v) water-ethanol mixture was sonicated for 2
100   hours to ensure uniform dispersion and prevent aggregation. A glassy carbon electrode (GCE, 3
101   mm diameter) was polished with 50 nm aqueous alumina slurry on a polishing cloth to enhance
102   surface roughness and cleaned via ultrasonication in ethanol and water. The cleaned GCE was
103   dried under a nitrogen gas stream to avoid contamination.

104   *CNT Deposition and Gold Nanoparticle (AuNP) Coating*   5 µL of the CNT suspension was
105   drop-cast onto the GCE surface and dried at room temperature to form a CNT-modified GCE
106   (CNTs/GCE). Gold nanoparticles (AuNPs) were electrochemically deposited onto the
107   CNTs/GCE by cycling the potential in a solution of gold (III) chloride hydrate solution in 0.5 M
108   H_2SO_4. The resulting AuNPs/CNTs/GCE served as the substrate for aptamer immobilization,
109   with AuNPs enhancing conductivity and providing a binding platform for thiolated aptamers.

110   *Aptamer Immobilization and Blocking*   A thiol-functionalized anti-SARS-CoV-2 S protein
111   aptamer solution was incubated on the AuNPs/CNTs/GCE for 1 hour at room temperature to
112   form a self-assembled monolayer. After aptamer immobilization, the electrode was rinsed with
113   phosphate-buffered saline (PBS, pH 7.4) to remove unbound aptamers. To prevent non-specific
114   binding, the surface of the electrode was treated with 0.05% BSA solution in PBS for 30
115   minutes, followed by rinsing with PBS. The aptamer/AuNPs/CNTs/GCE electrochemical
116   impedance aptasensor was stored at 4°C for further use.

2.4 Surface plasmon resonance

118   Binding kinetics were analyzed using a Biacore 2000 system at 25°C. The aptamer was
119   immobilized onto a Series S Sensor Chip SA (GE Healthcare) in a running buffer containing 10
120   mM HEPES, 150 mM NaCl, pH 7.4, and 0.005% (v/v) Tween-20. Serial dilutions of the SARS-
121   CoV-2 S protein were injected at a flow rate of 30 µL/min, with association and dissociation
122   phases lasting 180 seconds and 900 seconds, respectively. Regeneration of the chip surface was
123   achieved using 0.1 M glycine-HCl buffer (pH 2) applied in two 10-second intervals. The
124   optimized buffer composition ensured aptamer stability and reproducible sensor performance
125   across cycles.

2.5 Negative-stain sample preparation and microscopy

Aptamer-conjugated AuNPs were incubated with SARS-CoV-2 S protein on ice for 30 minutes at a 1:1 molar ratio. Glow-discharged Formvar-coated copper electron microscopy (EM) grids (Electron Microscopy Sciences, USA) were prepared by applying the sample for one minute, blotting excess liquid, then washing three times with 2% uranyl acetate. A final incubation with uranyl acetate for one minute provided contrast for imaging. Grids were dried at room temperature and imaged at 15,000x magnification using a Tecnai T12 microscope (Thermo Fisher Scientific, USA). Control samples, prepared using the same protocol without aptamers, were used to verify specificity.

2.6 Cryo-EM sample preparation and imaging

The aptamer was incubated with thawed SARS-CoV-2 S protein (500µg/dL) on ice for 30 minutes at a 4:1 molar ratio. A 4 µl aliquot of sample was applied to holey carbon Quantifoil R2/1 copper 200-mesh grids (Electron Microscopy Sciences, USA), blotted, and vitrified using a Vitrobot Mark IV (Thermo Fisher Scientific, USA) in a liquid ethane/propane mixture. Grids were screened in a Tecnai T20 (Thermo Fisher Scientific, USA) transmission electron microscope to optimize freezing conditions.

Cryo-EM data was collected on a 300 kV Titan Krios (Thermo Fisher Scientific, USA) equipped with K3 direct electron detector (Gatan, USA) operated in electron counting mode. Movies were recorded at 81,000× magnification with a dose rate of 26.97 e$^-$ pixel^{-1} s^{-1}. A total of 12,834 movies were captured, each comprising 40 frames with a total exposure time of 2 seconds. Automated image acquisition was accomplished using SerialEM (Mastronarde 2018).

2.7 Data processing and 3D reconstruction

Data processing for 3D reconstruction was processed using CryoSPARC v4.3.1 and RELION-4.1 (Punjani et al. 2017; Scheres 2012). Micrograph curation was performed to remove low-quality images before proceeding with particle picking. In total, 11,972 selected micrographs were subjected to patch motion correction using *MotionCor2* and CTF estimation using *GCTF* (Zhang 2016; Zheng et al. 2017).

A previously published closed conformation map EMD-30660 (Xu et al. 2021) was used as a reference to generate templates for automated picking using *Template Picker* in CryoSPARC. These automatically picked particles were then subjected to iterative 2D classification, where the best classes were selected as templates for a second round of particle picking and subsequent 2D classification. The best classes were used to train a Topaz model (Bepler et al. 2019) for improved S protein particle picking. The trained Topaz model picked 1,175,879 particles, which were extracted at a box size of 330 Å (300 pixels) and filtered through additional rounds of 2D classification to remove junk particles, yielding a final dataset of 671,570 particles.

One round of homogeneous refinement on the extracted particles showed poorly resolved RBD densities in the resulting map, indicating multiple S protein conformations being averaged together. To resolve these different map conformations, we subsequently performed 3D classification on the newly extracted particles and specified 10 different classes. All 10 classes

166 were then subjected to heterogenous refinement with the previous 3D classification volumes as
167 references, revealing two major classes corresponding to the open and closed conformation
168 maps, respectively. The other classes from this heterogenous refinement step were poorly aligned
169 or appeared to be missing spike protein density, so we decided to discard them. The two major
170 classes were then subjected to another round of heterogeneous refinement to remove more bad
171 quality particles contributing to the two major conformations maps. One round of non-uniform
172 refinement (Punjani et al. 2020) in C1 symmetry was performed for both open and closed maps,
173 followed by a C3 refinement for the closed conformation due to its symmetrical positioning of
174 the down RBDs. This helped improve the resolution of the closed conformation map to 3.4 Å
175 (Table S1).

176   To better resolve the aptamer-RBD interaction in the open conformation, additional data
177 processing was carried out in RELION. A round of 3D classification was conducted on the entire
178 structure to remove particles corresponding to closed and misaligned conformations, followed by
179 a final round of global refinement. This refinement revealed a low-resolution helical density with
180 distinct grooves binding to the top of the open confirmation up RBD. Since this density aligned
181 well with our aptamer model, we confidently assigned it as the aptamer. To mitigate preferred
182 orientation artifacts in the open conformation map, anisotropic and misalignment correction
183 modules in *spIsoNet* (Liu et al. 2025) were applied. Sharpening and postprocessing were
184 performed on the half-maps generated from spIsoNet, yielding a final open confirmation map at
185 4.4 Å resolution (Table S1).

186   To assess structural variability of the up RBD in the open conformation, 3D variability
187 analysis (Punjani and Fleet 2021) was conducted in CryoSPARC, performed across three
188 different modes with the "filter resolution (Å)" parameter set at 6 Å. A total of 20 volumes per
189 mode was generated and volumes were downsampled to 150px, capturing dynamic structural
190 changes within the dataset. These volumes were compiled into a movie to visualize motion and
191 flexibility (Movie S1), providing deeper insights into conformational dynamics and potential
192 interactions.

2.8 Atomic model building and refinement

194 Initial model building was performed in Coot-0.8.9 (Emsley et al. 2010) and ISOLDE (Croll
195 2018) using sharpened maps for both conformations: the open conformation model was adapted
196 from PDB 7ND9 (Dejnirattisai et al. 2021) and the closed conformation model was derived from
197 PDB 7DF3 (Xu et al. 2021). Models of the open conformation were flexibly fitted into our 3D
198 variability maps to track positional changes of the up RBD. Model building of the aptamer
199 structure was based on initial AlphaFold3 (Abramson et al. 2024) prediction of CoV2-6C3
200 sequence, which was further refined to ensure correct base pairing of the aptamer. Following
201 initial model building, amino acid residues of the S protein and nucleotides of the aptamer were
202 both fixed via positional restraints. However, RBD residues involved in nucleotide recognition
203 and interaction, along with nucleotides predicted to interact with the RBD based on position and
204 literature, were released from these constraints, along with their neighboring residues (Sun et al.
205 2021). Potential RBD-aptamer interactions were simulated by implementing appropriate distance
206 restraints for noncovalent forces between the aforementioned amino acids and nucleotides. Our
207 ISOLDE simulation allowed us to flip out nucleotide bases and flexibly model non-covalent
208 interactions with the aptamer residues that conformed to our density map contact points. Final

209 refinements were performed in ISOLDE to optimize interactions between the aptamer and the
210 open RBD. Structure visualization and figure preparation were done with UCSF ChimeraX
211 (Meng et al. 2023).

3. Results

3.1 Development and performance of an electrochemical aptasensor for SARS-CoV-2 detection

213
214

215 The global urgency for rapid, sensitive, and scalable diagnostic tools has driven advancements in
216 biosensor technology. Towards this end, we set out to develop an electrochemical impedance
217 aptamer-based biosensor device, or aptasensor, leveraging a therapeutic aptamer sequence that
218 targets the RBD of the SARS-CoV-2 S protein. To maximize detection range of the aptasensor,
219 carbon nanotubes (CNTs) were used as base electrodes due to their large specific surface area to
220 better facilitate aptamer conjugation onto electrochemically deposited gold nanoparticles
221 (AuNPs) (Fig. 1a). Electrochemical impedance spectroscopy (EIS) was used to monitor the
222 charge-transfer resistance (R_{ct}) values, modeled using the Randles equivalent circuit model (Fig.
223 1b) (Vivier and Orazem 2022). Nyquist plots (Fig. 1b) revealed a semicircular region indicative
224 of charge-transfer limitation at high frequencies, and a linear portion corresponding to diffusion-
225 limitation at low frequencies (Vivier and Orazem 2022). The R_{ct} values increased proportionally
226 with SARS-CoV-2 S protein concentrations, demonstrating specific adsorption and subsequent
227 charge-transfer impedance in the presence of the $[Fe (CN)_6]^{3-/4-}$ redox probe. The aptasensor
228 achieved a detection range of 1 pg mL^{-1} to 10^5 pg mL^{-1}, with a strong linear correlation ($R^2 =$
229 0.995) (Fig. 1c) and a limit of detection (LOD) of 0.19 pg mL^{-1} (S/N = 3). This performance
230 reflects the synergistic impact of CNT-enhanced sensitivity and aptamer specificity (Wongkaew
231 et al. 2018). Notably, the biologically significant serum S protein concentration, reported as 33.9
232 ±22.4 pg/mL (Yonker et al. 2023), falls within the detection range of the aptasensor. Moreover,
233 the aptasensor detected SARS-CoV-2 S protein within one hour, highlighting its potential for
234 real-time diagnostics. The ability of the aptasensor to detect SARS-CoV-2 S protein with high
235 sensitivity and in a biologically relevant range underscores its practical utility.

236 To assess the binding kinetics and specificity of the aptamer, we employed surface
237 plasmon resonance (SPR). The SPR response increased proportionally with SARS-CoV-2 S
238 protein concentrations, confirming high-affinity binding between the aptamer and the S protein
239 (Figs. 1 d-h) (Hanke et al. 2022). Regeneration studies demonstrated that the aptasensor retained
240 binding efficiency across multiple cycles following treatment with a 0.1 M glycine-HCl buffer
241 (pH 2). This reversible binding is attributed to non-covalent forces, such as hydrogen bonding
242 and Van der Waals interactions (Williams et al. 2021), confirms the durability and cost-
243 effectiveness of the aptasensor for repeated diagnostic use. These findings highlight its strong
244 binding affinity, reusability, and potential as a scalable diagnostic platform for SARS-CoV-2 and
245 emerging pathogens.

3.2 Cryo-EM reveals aptamer-S protein interactions

247 We used immunogold labeling to confirm the presence of aptamer-conjugated AuNPs and
248 visualized their association with S protein via negative-stain EM (Fig. 2a). Initial cryo-EM
249 studies using lyophilized S protein revealed that it had lost its ability to interact with the aptamer.

250   To determine the structure of the aptamer-S protein complex, we recorded ~12,000 movies using
251   cryo-EM with liquid S protein and subjected our extracted S protein particles to single particle
252   analysis (Fig. 2b). Extensive 3D classification and heterogenous refinement revealed two major
253   classes with distinct differences in RBD positioning and aptamer interactions (Fig. 2c). We
254   designated these classes as open and closed conformations consistent with previous studies (Ye
255   et al. 2022). Further 3D refinement led to an open confirmation map at resolution 4.4 Å and a
256   closed conformation map at 3.4 Å.

257   The open conformation of the S protein consists of one RBD in an upright position (up
258   RBD) and two in the lying-down position (down RBD), with the aptamer bound to the up RBD.
259   The aptamer binds with the up RBD at two distinct locations, forming a bridge-like interaction
260   similar to the three-pointed hACE2 interaction model (Wrapp et al. 2020). Additionally, we
261   observed a second sickle-shaped density that binds within the cleft between the two down RBDs
262   and the one up RBD. In contrast, the closed conformation has all three RBDs in the down
263   position with no residues exposed for aptamer binding.

264   To gain further insight into RBD–aptamer interactions and positioning, we atomically
265   modeled the open and closed S protein conformations, assigning domains to our monomers
266   based on established literature: N-terminal Domain (14-305), RBD (319-541), C-terminal
267   Domain (541-685), Fusion Peptide (788-806), Heptapeptide Repeat Sequence 1 (908-984),
268   Central Helix (984-1035) and Connector Domain (1035-1146) (Yan et al. 2020) (Fig. 2d). Our
269   modeling of the S1 (residues 1–685) and S2 (residues 686–1164) subunits revealed that while the
270   S2 domains remain relatively rigid, the RBDs within S1 exhibit greater flexibility (Movie S1). In
271   the S1 domain, the up RBD is elevated ~ 3.7 nm from the down RBD, with an approximate 36°
272   angle separating the two RBD configurations and a 40° angle rotation out of the page (Fig. 2e).
273   These findings highlight the critical role of RBD movement and RBD exposure in aptamer
274   recognition, providing a structural framework to optimize aptamer-based detection strategies.

275   **3.3 Positional variability and interactions of aptamer-RBD complex**

276   The open conformation of the S protein binds the aptamer through its up RBD, forming a
277   complex that is nearly perpendicular to adjacent monomer NTDs. To characterize the flexibility
278   of this aptamer-RBD complex, we employed 3D Variability Analysis (3DVAR) in CryoSPARC
279   to model its movement relative to the rest of the S protein (Fig. 3a). Our results revealed that the
280   aptamer-RBD complex shifted up to 2 nm towards the adjacent RBD, transitioning from a
281   "straight" conformation to a "bent" conformation (Fig. 3b). Notably, the aptamer-RBD complex
282   transiently shifts between the straight and bent conformations, showing strong binding to both
283   conformations but reduced aptamer binding in the transition between them.

284   To further characterize the bridge-like interface between the aptamer and the RBD, we
285   modeled putative interactions at the C-terminal region (residues 445-490) and the N-terminal
286   region (residues 490-505) of the S protein RBD in the RBD-aptamer complex. Since our map
287   precluded atomic modeling of interactions at the aptamer-RBD interface, we leveraged ISOLDE,
288   a density-guided simulation software, to reveal potential binding mechanisms of the aptamer to
289   the RBD. ISOLDE simulations steered the fitting of both S protein residues and aptamer
290   nucleotides into the map, while considering noncovalent interactions (hydrogen bonds, ionic

291 interactions, and van der Waals forces) and maintaining geometry constraints (bond lengths and
292 angles) for protein and nucleic acid components. Based on our simulations, we propose that the
293 aptamer interacts with the C-terminal cluster of RBD amino acids Y489, N487, F486, and S477
294 via unpaired nucleotides A14 and A15, consistent with previous aptamer mutagenesis studies
295 (Sun et al. 2021) (Fig. 3c). At the N-terminal region, C6 likely interacts with N501, a residue
296 previously implicated in hydrogen bonding with hACE2 residues (Yan et al. 2020). While the
297 resolution in this region limits atomic modeling of nucleotide-residue interactions, we propose
298 aptamer binding occurs through a combination of hydrogen bonding between polar or charged
299 amino acids (e.g., N487 and S477) and unpaired nucleotides, along with π-stacking interactions
300 between unpaired bases and aromatic residues (e.g., F486) (Fig. 3c). Overall, these forces likely
301 strengthen binding affinity and maintain specificity of RBD-aptamer bridge contacts, even as the
302 complex changes position.

4. Discussion

303

304 In this study, we demonstrate that repurposing therapeutic aptamers provides a rapid and
305 effective strategy for designing biosensors to detect the SARS-CoV-2 S protein. Our
306 electrochemical aptasensor achieved high sensitivity and specificity for the SARS-CoV-2 S
307 protein's receptor-binding domain (RBD) within a biologically relevant detection range (Wrobel
308 2023; Zhu et al. 2020), demonstrating its potential for rapid and scalable diagnostic applications.
309 We used cryo-EM to further reveal the dynamics and specificity of our aptamer interaction with
310 the open conformation S protein. Notably, our study is the first to characterize low-resolution
311 aptamer binding to the RBD providing structural insights into aptamer-target interactions.

312 The up RBD in the open conformation undergoes dynamic positional changes that
313 influence aptamer binding. Our flexibility analysis for the up RBD aligns with prior molecular
314 dynamics (MD) simulations and 3D variability models, which indicate that the up RBD can
315 occupy a variety of different positions in the open conformation (Ye et al. 2022). Given that our
316 aptamer is significantly smaller than hACE2, it is reasonable to expect a greater number of
317 binding conformations for the aptamer-RBD interaction. In the presence of hACE2, the S protein
318 RBDs can adopt different positions that facilitate hACE2 binding and subsequent stabilization
319 (Yajima et al. 2024). Similarly, our aptamer-RBD complex has a stable interaction across
320 different flexible states of the up RBD. Additionally, as the RBD transitions from a straight to a
321 bent conformation, the sickle-shaped density between the RBDs becomes less pronounced, likely
322 due to the up RBD moving closer to the adjacent RBD in neighboring monomers. Interestingly,
323 this density is not present in the closed confirmation when all three RBDs are in the down
324 configuration. We suggest this density to be a poorly resolved potential secondary aptamer-
325 binding site in the open confirmation, as it roughly aligns with our aptamer model and localizes
326 near the aptamer-S protein-binding residues of the two down RBDs of adjacent monomers. In
327 conclusion, the dynamic flexibility of the up RBD allows for multiple aptamer binding
328 conformations, and our findings highlight the stability of the aptamer-RBD interaction across
329 different RBD positions, paralleling the behavior observed with hACE2 binding.

330 The visible connection between the aptamer and RBD densities allowed us to pose
331 several hypothetical models of interaction between the aptamer and the RBD. Our C-terminal
332 predictions are consistent with prior mutagenesis studies, highlighting the role of specific
333 residues - particularly F486 - in replicating established hACE2 interactions (Yan et al. 2020).
334 While previous MD simulations predicted the aptamer A17 as part of this C-terminal interface,

335 our density-guided simulations indicate that A17 does not contribute to the A14/A15 RBD
336 interface and may instead play a further structural role in coordinating with nearby residues or
337 nucleotides. Our RBD N-terminal interactions provide further support for residues T500 and
338 N501 in mimicking hACE2 binding to the aptamer (Boon et al. 2021). Given that key residues
339 along the C- and N-terminal regions of the RBD involved in aptamer recognition also play a role
340 in recognizing hACE2, our aptamer emerges as a strong candidate for competitively inhibiting
341 the S protein RBD, with the potential to displace hACE2 in vivo, as demonstrated by other
342 studies (Sun et al. 2021).

343 While our work highlights the sensitivity and detection mechanism of the aptasensor,
344 further research is necessary to fully harness the potential of DNA-based biosensors for future
345 pandemics. A key advantage of this technology is its regeneration capability, which could
346 significantly reduce operational costs and improve scalability (Goode et al. 2015). Additionally,
347 the minimal sample requirement of the aptasensor makes it particularly suitable for resource-
348 limited settings, supporting rapid, minimally invasive diagnostics that are crucial for scalable
349 outbreak responses (Broughton et al., 2020). Another advantage of the aptasensor is in its dose-
350 dependent detection, which enhances clinical utility by enabling accurate tracking of a patient's
351 condition through the detection of S protein at biologically relevant concentrations. Expanding
352 this approach, the aptamer could be adapted to target biomarkers such as acute-phase reactants
353 and immunoglobulins, allowing clinicians to monitor disease progression and treatment efficacy,
354 particularly in cases with fluctuating viral loads (Shanmugaraj et al., 2020). Beyond its
355 diagnostic applications, the aptamer may also modulate S protein accessibility, potentially
356 influencing viral entry and immune recognition. Future studies should focus on quantifying its
357 binding kinetics relative to hACE2 and assessing its impact on S protein behavior under
358 physiological conditions to further explore its therapeutic potential.

5. Conclusion

360 In summary, we have developed a DNA-based aptasensor for the detection of the SARS-CoV-2
361 S protein, demonstrating high sensitivity, specificity, and reusability. The aptasensor achieves
362 detection within one hour, operating within biologically relevant S protein concentrations,
363 underscoring its potential for real-time diagnostics. Our structural analysis provides insights into
364 aptamer-RBD interactions, revealing a bridge-like binding mechanism and the flexible nature of
365 the aptamer-RBD complex. While further optimization and clinical validation are needed, the
366 combination of sensitivity, specificity, and scalability establishes aptasensors as promising tools
367 for next-generation diagnostics and pandemic preparedness.

CRediT author contribution statement

369 Yujun Liu: Conceptualization, Data curation, Formal analysis, Investigation, Visualization,
370 Writing – original draft, Writing – review & editing. Kaidong Wang: Conceptualization, Data
371 curation, Formal analysis, Investigation, Visualization, Writing – original draft, Writing – review
372 & editing. Weiguang Wang: Formal analysis, Visualization, Writing – original draft, Writing –
373 review & editing. Saarang Kashyap: Formal analysis, Visualization, Writing – original draft,
374 Writing – review & editing. Jonathan Jih: Formal analysis, Writing – review & editing. Anthony
375 Imani: Formal analysis, Visualization, Writing – original draft, Writing – review & editing.
376 Tzung K. Hsiai: Conceptualization, Methodology, Supervision, Writing – review & editing,

377 Funding acquisition, Resources. Z. Hong Zhou: Conceptualization, Methodology, Project
378 administration, Supervision, Writing – original draft, Writing – review & editing, Funding
379 acquisition, Resources. All authors reviewed and approved of the paper.

Declaration of competing interest

381 The authors declare no competing interests.

Acknowledgments

Funding

Additional information

395 All data needed to evaluate the conclusions in the paper are present in the paper and/or the
396 Supplementary Information. Additional data related to this paper may be requested from the
397 authors. Cryo-EM density maps and 3D models are deposited in EMDB and PDB under the
398 accession numbers EMD-XXXXX and XXXX, respectively.
399

References

401 Abramson, J., Adler, J., Dunger, J., Evans, R., Green, T., Pritzel, A., Ronneberger, O., Willmore, L.,
402 Ballard, A.J., Bambrick, J., Bodenstein, S.W., Evans, D.A., Hung, C.-C., O'Neill, M., Reiman, D.,
403 Tunyasuvunakool, K., Wu, Z., Žemgulytė, A., Arvaniti, E., Beattie, C., Bertolli, O., Bridgland, A.,
404 Cherepanov, A., Congreve, M., Cowen-Rivers, A.I., Cowie, A., Figurnov, M., Fuchs, F.B., Gladman, H.,
405 Jain, R., Khan, Y.A., Low, C.M.R., Perlin, K., Potapenko, A., Savy, P., Singh, S., Stecula, A.,
406 Thillaisundaram, A., Tong, C., Yakneen, S., Zhong, E.D., Zielinski, M., Žídek, A., Bapst, V., Kohli, P.,
407 Jaderberg, M., Hassabis, D., Jumper, J.M., 2024. Accurate structure prediction of biomolecular
408 interactions with AlphaFold 3. Nature 630(8016), 493-500.
409
410 Artika, I.M., Dewi, Y.P., Nainggolan, I.M., Siregar, J.E., Antonjaya, U., 2022. Real-Time Polymerase
411 Chain Reaction: Current Techniques, Applications, and Role in COVID-19 Diagnosis. Genes (Basel)
412 13(12).
413
414 Bashir, A., Yang, Q., Wang, J., Hoyer, S., Chou, W., McLean, C., Davis, G., Gong, Q., Armstrong, Z.,
415 Jang, J., Kang, H., Pawlosky, A., Scott, A., Dahl, G.E., Berndl, M., Dimon, M., Ferguson, B.S., 2021.
416 Machine learning guided aptamer refinement and discovery. Nature Communications 12(1), 2366.
417

418 Benton, D.J., Wrobel, A.G., Xu, P., Roustan, C., Martin, S.R., Rosenthal, P.B., Skehel, J.J., Gamblin, S.J.,
419 2020. Receptor binding and priming of the spike protein of SARS-CoV-2 for membrane fusion. Nature
420 588(7837), 327-330.
421
422 Bepler, T., Morin, A., Rapp, M., Brasch, J., Shapiro, L., Noble, A.J., Berger, B., 2019. Positive-unlabeled
423 convolutional neural networks for particle picking in cryo-electron micrographs. Nature Methods 16(11),
424 1153-1160.
425
426 Boon, S.S., Xia, C., Wang, M.H., Yip, K.L., Luk, H.Y., Li, S., Ng, R.W.Y., Lai, C.K.C., Chan, P.K.S.,
427 Chen, Z., 2021. Temporal-Geographical Dispersion of SARS-CoV-2 Spike Glycoprotein Variant Lineages
428 and Their Functional Prediction Using <i>in Silico</i> Approach. mBio 12(5), 10.1128/mbio.02687-
429 02621.
430
431 Cai, Y., Zhang, J., Xiao, T., Peng, H., Sterling, S.M., Walsh, R.M., Rawson, S., Rits-Volloch, S., Chen, B.,
432 2020. Distinct conformational states of SARS-CoV-2 spike protein. Science 369(6511), 1586-1592.
433
434 Chen, Z., Hu, L., Zhang, B.T., Lu, A., Wang, Y., Yu, Y., Zhang, G., 2021. Artificial Intelligence in
435 Aptamer-Target Binding Prediction. Int J Mol Sci 22(7).
436
437 Croll, T., 2018. ISOLDE: a physically realistic environment for model building into low-resolution
438 electron-density maps. Acta Crystallographica Section D 74(6), 519-530.
439
440 Dejnirattisai, W., Zhou, D., Ginn, H.M., Duyvesteyn, H.M.E., Supasa, P., Case, J.B., Zhao, Y., Walter,
441 T.S., Mentzer, A.J., Liu, C., Wang, B., Paesen, G.C., Slon-Campos, J., López-Camacho, C., Kafai, N.M.,
442 Bailey, A.L., Chen, R.E., Ying, B., Thompson, C., Bolton, J., Fyfe, A., Gupta, S., Tan, T.K., Gilbert-
443 Jaramillo, J., James, W., Knight, M., Carroll, M.W., Skelly, D., Dold, C., Peng, Y., Levin, R., Dong, T.,
444 Pollard, A.J., Knight, J.C., Klenerman, P., Temperton, N., Hall, D.R., Williams, M.A., Paterson, N.G.,
445 Bertram, F.K.R., Siebert, C.A., Clare, D.K., Howe, A., Radecke, J., Song, Y., Townsend, A.R., Huang, K.-
446 Y.A., Fry, E.E., Mongkolsapaya, J., Diamond, M.S., Ren, J., Stuart, D.I., Screaton, G.R., 2021. The
447 antigenic anatomy of SARS-CoV-2 receptor binding domain. Cell 184(8), 2183-2200.e2122.
448
449 Emsley, P., Lohkamp, B., Scott, W.G., Cowtan, K., 2010. Features and development of Coot. Acta
450 Crystallogr D Biol Crystallogr 66(Pt 4), 486-501.
451
452 Goode, J.A., Rushworth, J.V.H., Millner, P.A., 2015. Biosensor Regeneration: A Review of Common
453 Techniques and Outcomes. Langmuir 31(23), 6267-6276.
454
455 Hanke, L., Das, H., Sheward, D.J., Perez Vidakovics, L., Urgard, E., Moliner-Morro, A., Kim, C., Karl,
456 V., Pankow, A., Smith, N.L., 2022. A bispecific monomeric nanobody induces spike trimer dimers and
457 neutralizes SARS-CoV-2 in vivo. Nature communications 13(1), 155.
458
459 Hoffmann, M., Kleine-Weber, H., Pöhlmann, S., 2020. A Multibasic Cleavage Site in the Spike Protein of
460 SARS-CoV-2 Is Essential for Infection of Human Lung Cells. Mol Cell 78(4), 779-784.e775.
461
462 Justino, C.I.L., Duarte, A.C., Rocha-Santos, T.A.P., 2016. Critical overview on the application of sensors
463 and biosensors for clinical analysis. TrAC Trends in Analytical Chemistry 85, 36-60.
464
465 Khan, S.H., Zaidi, S.K., Gilani, M., 2022. PCR to CRISPR: Role of Nucleic Acid Tests (NAT) in
466 detection of COVID-19. J Pak Med Assoc 72(6), 1166-1174.
467

Kumar Kulabhusan, P., Hussain, B., Yüce, M., 2020. Current Perspectives on Aptamers as Diagnostic Tools and Therapeutic Agents. Pharmaceutics 12(7).

Liu, Y.T., Fan, H., Hu, J.J., Zhou, Z.H., 2025. Overcoming the preferred-orientation problem in cryo-EM with self-supervised deep learning. Nat Methods 22(1), 113-123.

Mastronarde, D.N., 2018. Advanced Data Acquisition From Electron Microscopes With SerialEM. Microscopy and Microanalysis 24(S1), 864-865.

Meng, E.C., Goddard, T.D., Pettersen, E.F., Couch, G.S., Pearson, Z.J., Morris, J.H., Ferrin, T.E., 2023. UCSF ChimeraX: Tools for structure building and analysis. Protein Science 32(11), e4792.

Patel, S.K., Surve, J., Parmar, J., Ahmed, K., Bui, F.M., Al-Zahrani, F.A., 2023. Recent Advances in Biosensors for Detection of COVID-19 and Other Viruses. IEEE Rev Biomed Eng 16, 22-37.

Perumal, V., Hashim, U., 2014. Advances in biosensors: Principle, architecture and applications. Journal of Applied Biomedicine 12(1), 1-15.

Pohanka, M., 2018. Overview of Piezoelectric Biosensors, Immunosensors and DNA Sensors and Their Applications. Materials (Basel) 11(3).

Punjani, A., Fleet, D.J., 2021. 3D variability analysis: Resolving continuous flexibility and discrete heterogeneity from single particle cryo-EM. Journal of Structural Biology 213(2), 107702.

Punjani, A., Rubinstein, J.L., Fleet, D.J., Brubaker, M.A., 2017. cryoSPARC: algorithms for rapid unsupervised cryo-EM structure determination. Nature Methods 14(3), 290-296.

Punjani, A., Zhang, H., Fleet, D.J., 2020. Non-uniform refinement: adaptive regularization improves single-particle cryo-EM reconstruction. Nature Methods 17(12), 1214-1221.

Samson, R., Navale, G.R., Dharne, M.S., 2020. Biosensors: frontiers in rapid detection of COVID-19. 3 Biotech 10(9), 385.

Scheres, S.H.W., 2012. RELION: Implementation of a Bayesian approach to cryo-EM structure determination. Journal of Structural Biology 180(3), 519-530.

Sefah, K., Shangguan, D., Xiong, X., O'Donoghue, M.B., Tan, W., 2010. Development of DNA aptamers using Cell-SELEX. Nature Protocols 5(6), 1169-1185.

Shang, J., Wan, Y., Luo, C., Ye, G., Geng, Q., Auerbach, A., Li, F., 2020. Cell entry mechanisms of SARS-CoV-2. Proceedings of the National Academy of Sciences 117(21), 11727-11734.

Shi, R., Shan, C., Duan, X., Chen, Z., Liu, P., Song, J., Song, T., Bi, X., Han, C., Wu, L., Gao, G., Hu, X., Zhang, Y., Tong, Z., Huang, W., Liu, W.J., Wu, G., Zhang, B., Wang, L., Qi, J., Feng, H., Wang, F.-S., Wang, Q., Gao, G.F., Yuan, Z., Yan, J., 2020. A human neutralizing antibody targets the receptor-binding site of SARS-CoV-2. Nature 584(7819), 120-124.

Sun, M., Liu, S., Wei, X., Wan, S., Huang, M., Song, T., Lu, Y., Weng, X., Lin, Z., Chen, H., Song, Y., Yang, C., 2021. Aptamer Blocking Strategy Inhibits SARS-CoV-2 Virus Infection. Angew Chem Int Ed Engl 60(18), 10266-10272.

519 Vivier, V., Orazem, M.E., 2022. Impedance analysis of electrochemical systems. Chemical Reviews
520 122(12), 11131-11168.
521
522 Walls, A.C., Park, Y.J., Tortorici, M.A., Wall, A., McGuire, A.T., Veesler, D., 2020. Structure, Function,
523 and Antigenicity of the SARS-CoV-2 Spike Glycoprotein. Cell 181(2), 281-292.e286.
524
525 Williams, G.T., Haynes, C.J., Fares, M., Caltagirone, C., Hiscock, J.R., Gale, P.A., 2021. Advances in
526 applied supramolecular technologies. Chemical Society Reviews 50(4), 2737-2763.
527
528 Wongkaew, N., Simsek, M., Griesche, C., Baeumner, A.J., 2018. Functional nanomaterials and
529 nanostructures enhancing electrochemical biosensors and lab-on-a-chip performances: recent progress,
530 applications, and future perspective. Chemical reviews 119(1), 120-194.
531
532 Wrapp, D., Wang, N., Corbett, K.S., Goldsmith, J.A., Hsieh, C.-L., Abiona, O., Graham, B.S., McLellan,
533 J.S., 2020. Cryo-EM structure of the 2019-nCoV spike in the prefusion conformation. Science 367(6483),
534 1260-1263.
535
536 Wrobel, A.G., 2023. Mechanism and evolution of human ACE2 binding by SARS-CoV-2 spike. Curr
537 Opin Struct Biol 81, 102619.
538
539 Xia, S., Liu, M., Wang, C., Xu, W., Lan, Q., Feng, S., Qi, F., Bao, L., Du, L., Liu, S., Qin, C., Sun, F., Shi,
540 Z., Zhu, Y., Jiang, S., Lu, L., 2020. Inhibition of SARS-CoV-2 (previously 2019-nCoV) infection by a
541 highly potent pan-coronavirus fusion inhibitor targeting its spike protein that harbors a high capacity to
542 mediate membrane fusion. Cell Research 30(4), 343-355.
543
544 Xu, C., Wang, Y., Liu, C., Zhang, C., Han, W., Hong, X., Wang, Y., Hong, Q., Wang, S., Zhao, Q., Wang,
545 Y., Yang, Y., Chen, K., Zheng, W., Kong, L., Wang, F., Zuo, Q., Huang, Z., Cong, Y., 2021.
546 Conformational dynamics of SARS-CoV-2 trimeric spike glycoprotein in complex with receptor ACE2
547 revealed by cryo-EM. Science Advances 7(1), eabe5575.
548
549 Yajima, H., Anraku, Y., Kaku, Y., Kimura, K.T., Plianchaisuk, A., Okumura, K., Nakada-Nakura, Y.,
550 Atarashi, Y., Hemmi, T., Kuroda, D., Takahashi, Y., Kita, S., Sasaki, J., Sumita, H., Matsuno, K., Nao, N.,
551 Sawa, H., Mizuma, K., Li, J., Kida, I., Mimura, Y., Ohari, Y., Tanaka, S., Tsuda, M., Wang, L., Oda, Y.,
552 Ferdous, Z., Shishido, K., Mohri, H., Iida, M., Fukuhara, T., Tamura, T., Suzuki, R., Suzuki, S., Tsujino,
553 S., Ito, H., Misawa, N., Guo, Z., Hinay, A.A., Usui, K., Saikruang, W., Lytras, S., Uriu, K., Yoshimura, R.,
554 Kawakubo, S., Nishumura, L., Kosugi, Y., Fujita, S., M.Tolentino, J.E., Chen, L., Pan, L., Li, W., Yo,
555 M.S., Horinaka, K., Suganami, M., Chiba, M., Yasuda, K., Iida, K., Strange, A.P., Ohsumi, N., Tanaka, S.,
556 Ogawa, E., Fukuda, T., Osujo, R., Yoshimura, K., Sadamas, K., Nagashima, M., Asakura, H., Yoshida, I.,
557 Nakagawa, S., Takayama, K., Hashimoto, R., Deguchi, S., Watanabe, Y., Nakata, Y., Futatsusako, H.,
558 Sakamoto, A., Yasuhara, N., Suzuki, T., Nakajima, Y., Irie, T., Kawabata, R., Sasaki-Tabata, K., Ikeda, T.,
559 Nasser, H., Shimizu, R., Begum, M.S.T.M., Jonathan, M., Mugita, Y., Leong, S., Takahashi, O., Ueno, T.,
560 Motozono, C., Toyoda, M., Saito, A., Kosaka, A., Kawano, M., Matsubara, N., Nishiuchi, T., Zahradnik,
561 J., Andrikopoulos, P., Padilla-Blanco, M., Konar, A., Ito, J., Maenaka, K., Sato, K., Hashiguchi, T., The
562 Genotype to Phenotype Japan, C., 2024. Structural basis for receptor-binding domain mobility of the
563 spike in SARS-CoV-2 BA.2.86 and JN.1. Nature Communications 15(1), 8574.
564
565 Yan, R., Zhang, Y., Li, Y., Xia, L., Guo, Y., Zhou, Q., 2020. Structural basis for the recognition of SARS-
566 CoV-2 by full-length human ACE2. Science 367(6485), 1444-1448.
567
568 Ye, G., Liu, B., Li, F., 2022. Cryo-EM structure of a SARS-CoV-2 omicron spike protein ectodomain.
569 Nature Communications 13(1), 1214.

570

571 Yonker, L.M., Swank, Z., Bartsch, Y.C., Burns, M.D., Kane, A., Boribong, B.P., Davis, J.P., Loiselle, M.,
572 Novak, T., Senussi, Y., Cheng, C.A., Burgess, E., Edlow, A.G., Chou, J., Dionne, A., Balaguru, D.,
573 Lahoud-Rahme, M., Arditi, M., Julg, B., Randolph, A.G., Alter, G., Fasano, A., Walt, D.R., 2023.
574 Circulating Spike Protein Detected in Post-COVID-19 mRNA Vaccine Myocarditis. Circulation 147(11),
575 867-876.

576

577 Zhang, K., 2016. Gctf: Real-time CTF determination and correction. Journal of Structural Biology 193(1),
578 1-12.

579

580 Zheng, S.Q., Palovcak, E., Armache, J.P., Verba, K.A., Cheng, Y., Agard, D.A., 2017. MotionCor2:
581 anisotropic correction of beam-induced motion for improved cryo-electron microscopy. Nat Methods
582 14(4), 331-332.

583

584 Zhu, N., Zhang, D., Wang, W., Li, X., Yang, B., Song, J., Zhao, X., Huang, B., Shi, W., Lu, R., Niu, P.,
585 Zhan, F., Ma, X., Wang, D., Xu, W., Wu, G., Gao, G.F., Tan, W., 2020. A Novel Coronavirus from Patients
586 with Pneumonia in China, 2019. N Engl J Med 382(8), 727-733.
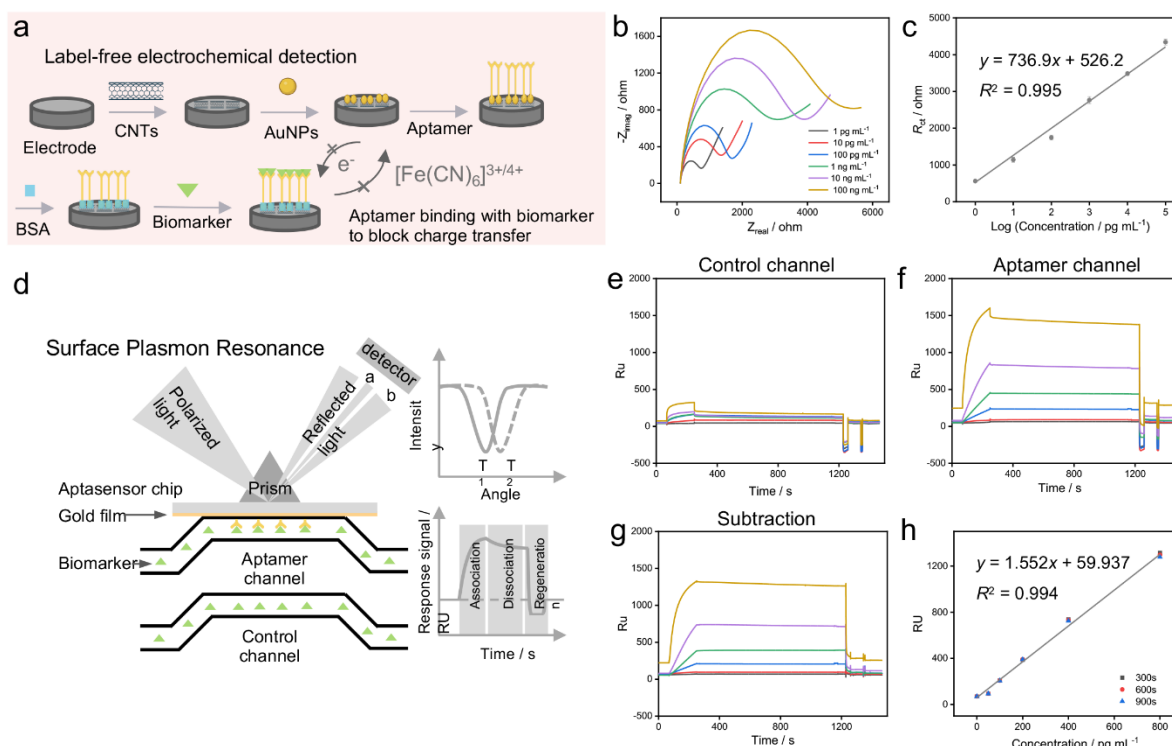
587

588 **Figure Legends:**

589
590 **Figure 1. Development and performance of aptasensor for SARS-CoV-2 S protein detection.** (**a**)
591 Schematic representation of the electrochemical impedance aptasensor fabrication process using carbon
592 nanotubes (CNTs), gold nanoparticles (AuNPs), and an anti-SARS-CoV-2 S protein aptamer for selective
593 detection. (**b**) Electrochemical impedance spectroscopy (EIS) responses at different concentrations of
594 SARS-CoV-2 S protein, ranging from 1 pg/mL to 10^5 pg/mL. (**c**) Calibration curve for correlating EIS
595 response (R_{ct} values) with SARS-CoV-2 S protein concentrations, fitted using the Randles equivalent
596 circuit model. (**d**) Diagram illustrating the working principle of surface plasmon resonance (SPR)
597 detection for SARS-CoV-2 S protein detection using an aptamer-modified microfluidic chip. (**e**) SPR
598 signal response recorded in the control channel without aptamer modification, indicating nonspecific
599 adsorption. (**f**) SPR signal response observed in the aptamer functionalized channel, demonstrating
600 specific binding to the SARS-CoV-2 S protein. (**g**) Subtracted SPR signal response to highlight the
601 specific detection of the SARS-CoV-2 S protein by eliminating background signals from the control
602 channels. (**h**) Calibration curve for SPR responses at different concentrations of SARS-CoV-2 S protein.
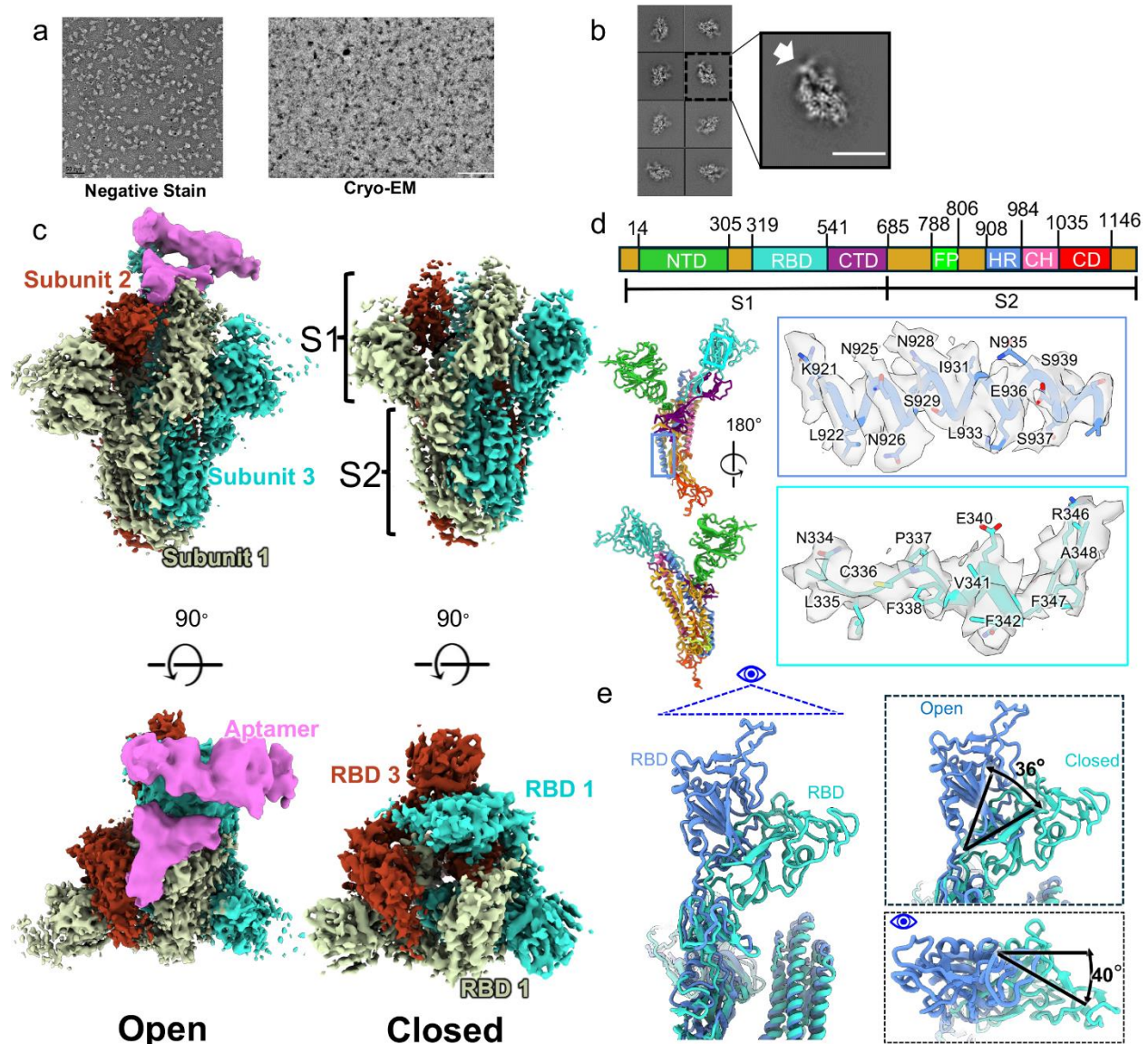603

Figure 2. Structural analysis of aptamer binding to SARS-CoV-2 S protein trimer. (**a**) Representative micrographs of negative-stain microscopy of aptamer-conjugated gold nanoparticles bound to S protein (Scale bar: 50 nm) and of cryo-EM of aptamer-S protein complexes (Scale bar: 100 nm). (**b**) Representative 2D class averages of aptamer-S protein complexes in cryo-EM images, with aptamer density interfacing with the receptor-binding domain (RBD) indicated by a white arrow. Scale bar: 135 Å (**c**) Maps of the S protein in open and closed conformations, with the aptamer densities in pink. (**d**) Labeled domains of full-length SARS-CoV-2 S protein. The S1 subunit contains NTD, RBD, and CTD, while S2 contains FP, HR1, CH, and CD. (**e**) Comparison of RBD positioning between open and closed conformations.
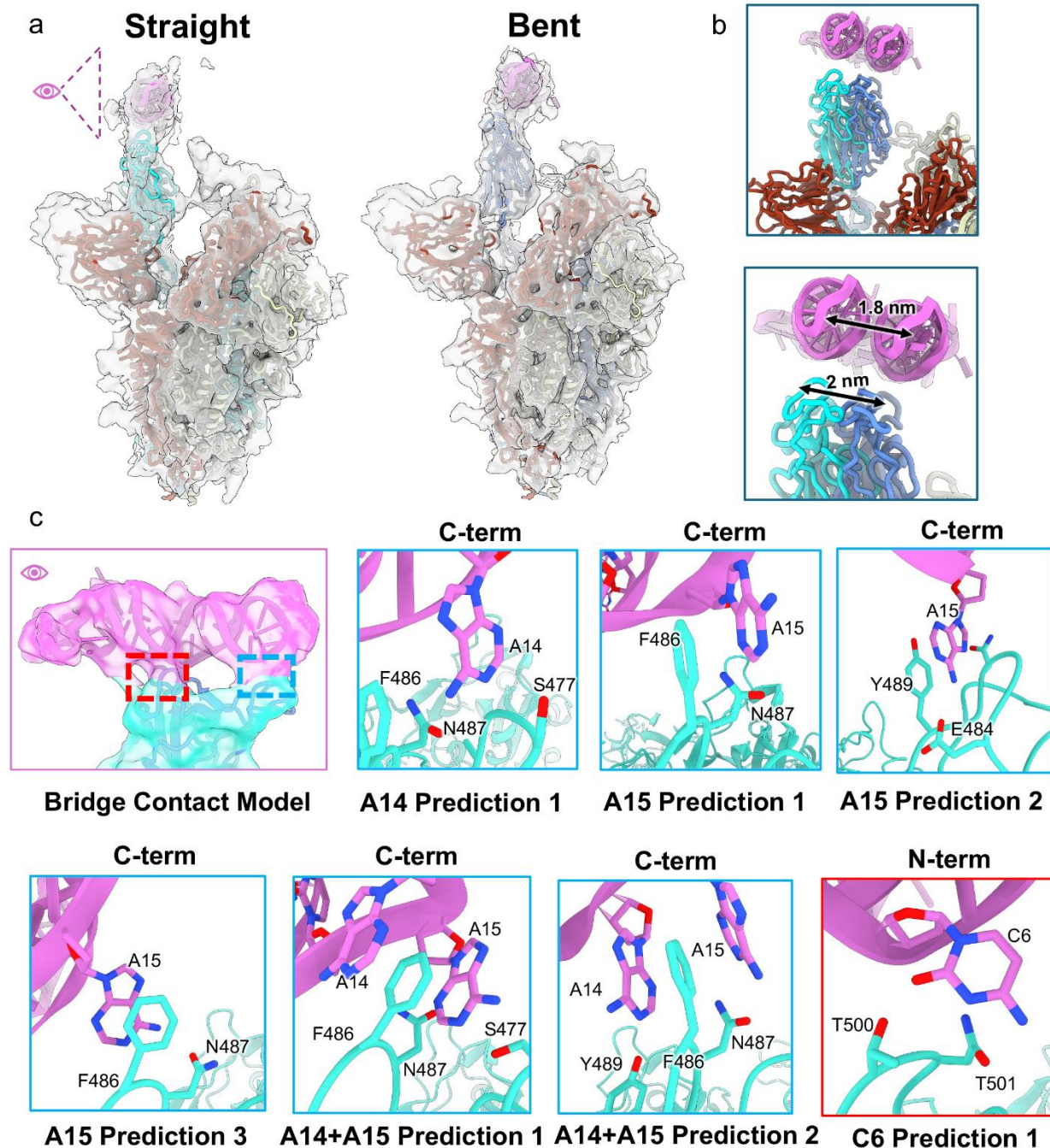
Figure 3. Flexibility of aptamer-RBD complex and density-guided simulations of aptamer binding interactions. (**a**) 3D Flexibility of the open conformation in the Straight and Bent positions. (**b**) shift in the aptamer-RBD position from straight to bent conformation. (**c**) Density-guided ISOLDE simulations of interactions between aptamer nucleotides and RBD residues at the C- and N-terminal regions of the RBD.